

The effect of electric and chiral magnetic conductivities on azimuthally fluctuating electromagnetic fields and observables in isobar collisions

Irfan Siddique^{1,*} and Uzma Tabassam²

¹*School of Nuclear Science and Technology, University of Chinese Academy of Sciences, Beijing 101408, China*

²*Department of Physics, COMSATS University Islamabad Campus, Islamabad, Park Road, 44000 Pakistan*

We study the space-time evolution of electromagnetic fields along with the azimuthal fluctuations of these fields and their correlation with the initial matter geometry specified by the participant plane in the presence of finite electric (σ) and chiral magnetic (σ_χ) conductivities in Ru+Ru and Zr+Zr collisions at $\sqrt{s_{NN}} = 200$ GeV. We observe the partially asymmetric behavior of the spatial distributions of the electric and magnetic fields in a conducting medium when compared to the Lienard-Wiechert (L-W) solutions, and deceleration of the decay of the fields is observed in both isobar collisions. While studying the correlation between the magnetic field direction and the participant plane, we see the sizeable suppression of the correlation in the presence of finite conductivities when compared to the L-W case, reflecting the importance of taking into account the medium properties such as conductivities while calculating the magnetic field induced observable quantities.

I. INTRODUCTION

The Ultra-relativistic heavy ion collision creates a deconfined state with extremely high energy and density known as Quark-Gluon-Plasma (QGP). In non-central heavy ion collisions, along with this high energy and density state, very strong electromagnetic fields are also generated due to charged particles having relativistic motions, which opens fortune to study related phenomenon in heavy ion collisions. Typical strength of magnetic field produced in heavy ion collisions can be estimated in co-moving frame for fast moving nuclei by $eB \sim \gamma Z e^2 / R_A^2$, with γ being the Lorentz Factor, Z being the proton number and R_A being the radius of the nucleus. For the case of Au+Au collisions at top RHIC (Relativistic Heavy ion collider) energies ($\sqrt{s_{NN}} = 200$ GeV) magnetic field is of orders of $eB \sim m_\pi^2 \sim 10^{18}$ Gauss [1–3] and fields are proportional to collision energy so at LHC (Large Hadron Collider) energies in Pb+Pb collisions at ($\sqrt{s_{NN}} = 2.76$ TeV) it can be roughly 10 times more stronger [4, 5]. In recent years, many developments and efforts have been made to explore the effects induced by (electro)magnetic fields such as the Chiral Magnetic Effect (CME) [6–11], the Chiral Separation Effects (CSE) [12, 13], Chiral Magnetic Wave (CMW) [14–18] etc. All of these effects are related to chiral fermions or massless fermions. Search for the CME is currently a very active field of interest in heavy ion collisions at the RHIC and LHC [19–25]. In early STAR and ALICE experiments charge separation effect was measured by measuring two particle azimuthal angle correlation $\gamma_{\alpha\beta} = \langle \cos(\phi_\alpha + \phi_\beta - 2\Psi_{RP}) \rangle$ with ϕ_i being the azimuthal angle of corresponding charged particle, α (β) denotes the sign of charge particle (either positive or negative) and Ψ_{RP} being the reaction plane angle, and the measurements support the presence of CME [19–21]. But

due to inseparable contribution from the background, it is extremely difficult to properly understand and extract the CME signal from the huge background in experiment results [23, 25–28]. There have been several attempts to eliminate or reduce background effects [29–32].

According to the expectations from CME, the difference between the correlation of opposite charge pairs ($\gamma_{opposite}$) and same charge pairs (γ_{same}) is expected to be directly proportional to the strength of the squared magnetic field $(e\mathbf{B})^2$ and azimuthal fluctuations of the magnetic field direction $(\cos 2(\Psi_B - \Psi_2))$ [33–35] i.e,

$$\Delta\gamma = \gamma_{opposite} - \gamma_{same} \propto \langle (e\mathbf{B})^2 \cos 2(\Psi_B - \Psi_2) \rangle \quad (1)$$

where Ψ_B represents the azimuthal angle of the magnetic field and Ψ_2 represents the second harmonic participant plane angle. The right hand side of the above equation shows that the quantitative contribution of the B-field-induced effect is essentially controlled by $(e\mathbf{B})^2 \cos 2(\Psi_B - \Psi_2)$, therefore this projected field strength controls the contribution rather than $(e\mathbf{B})^2$ alone.

To extract the CME signal, a solution proposed is to carry out isobaric collisions $\text{Ru}_{44}^{96} + \text{Ru}_{44}^{96}$ (Ru~Ruthenium) and $\text{Zr}_{40}^{96} + \text{Zr}_{40}^{96}$ (Zr~Zirconium) [36] and experiments were performed in RHIC [37–39] along this line to observe these effects. These isobaric collisions are intensely pursued for investigation because the advantage is that the difference in number of protons can generate different magnitudes of electromagnetic fields and related induced effects, but the same mass number in two isobar systems can generate the same background effect. So one can expect to observe the CME signal if it really exists in heavy ion collisions. For instance, from Woods-Saxon distributions it can be confirmed that in isobaric collisions $e\mathbf{B}$ differs by 10% [40], which naively agrees to the fact that the atomic number in Ru and Zr differ by 10% (Ru-44,Zr-40), so there can be a chance of observing a CME signal according to Eq. 1. Supposing that two isobar systems have same background then

* irfansiddique@ucas.ac.cn.edu.cn

$\Delta\gamma$ is expecting main contributions from the squared magnetic field and the correlation between the azimuthal angle of the magnetic field Ψ_B and participant plane Ψ_2 . So the first key ingredient is the fact that magnetic field whose spatial and time evolution in different mediums can behave differently [41–46], so consequently can have effect on related observables. So in this paper, we will study the electric and magnetic fields produced in isobar collisions in the presence of electric and chiral magnetic conductivities and measure their effect on the azimuthal fluctuations of electromagnetic fields and related observable quantities.

After providing the brief introduction, in Section II we give the expressions for electric and magnetic fields in zero conductivity system and system having finite conductivity. In Section III we provide simulation results and discussions for the electromagnetic fields and their correlation with initial matter geometry specified by the participant plane in central and non central isobaric collisions. Finally we summarize in Section IV.

II. CALCULATION OF ELECTROMAGNETIC FIELD

A: Zero-conductivity system ($\sigma = \sigma_\chi = 0$)

For a system with zero conductivity, or vacuum ($\sigma = \sigma_\chi = 0$), the electric and magnetic field in each event can be evaluated by using the Lienard-Wiechert potential [1, 33] as

$$\mathbf{E}(t, \mathbf{x}) = \alpha_{EM} \sum_n \frac{(1 - v_n^2) \mathbf{R}_n}{\left(\mathbf{R}_n^2 - (\mathbf{R}_n \times \mathbf{v}_n)^2\right)^{3/2}}, \quad (2)$$

$$\mathbf{B}(t, \mathbf{x}) = \alpha_{EM} \sum_n \frac{(1 - v_n^2) (\mathbf{v}_n \times \mathbf{R}_n)}{\left(\mathbf{R}_n^2 - (\mathbf{R}_n \times \mathbf{v}_n)^2\right)^{3/2}}, \quad (3)$$

where $\mathbf{R}_n = \mathbf{x} - \mathbf{x}_n$ is the relative position vector between the source point \mathbf{x}_n and the field point \mathbf{x} under discussion, and \mathbf{x}_n and \mathbf{v}_n represent the position and velocity respectively of the n -th proton in the colliding nuclei at the current time t . In above equation $\alpha_{EM} = e/4\pi \approx 1/137$ is fine structure constant. Note that the Eqs. (2) and (3) are valid under the assumption that all the source charges are traveling with a constant velocity. If all the charges do not have constant velocity then the original form of the Lienard-Wiechert fields [2, 45] using the retarded time should be used for the calculation of the electric and magnetic fields.

B: Conducting system with finite conductivities ($\sigma \neq 0, \sigma_\chi \neq 0$)

The quark-gluon plasma (QGP) matter is produced in heavy-ion collisions and it has certain conducting prop-

erty so it is important to take into account the feedback effects of the conductivities. The Maxwell equations with both electric (σ) and chiral magnetic (σ_χ) conductivities can be written in the following form:

$$\nabla \cdot \mathbf{F} = \begin{cases} \rho_{\text{ext}}/\epsilon & \rightarrow \mathbf{E} \\ 0 & \rightarrow \mathbf{B} \end{cases}, \quad (4)$$

$$\nabla \times \mathbf{F} = \begin{cases} -\partial_t \mathbf{B} & \rightarrow \mathbf{E} \\ \partial_t \mathbf{E} + \mathbf{J}_3(\sigma, \sigma_\chi) & \rightarrow \mathbf{B} \end{cases}, \quad (5)$$

where ρ_{ext} is external charge density and $\mathbf{J}_3(\sigma, \sigma_\chi) = \mathbf{J}_{\text{ext}} + \sigma \mathbf{E} + \sigma_\chi \mathbf{B}$ with \mathbf{J}_{ext} being external current density, $\sigma \mathbf{E}$ being electric current and $\sigma_\chi \mathbf{B}$ being chiral current, and \mathbf{F} denotes either electric (\mathbf{E}) or magnetic (\mathbf{B}) field. We can obtain the following algebraic expressions for electric and magnetic field components with finite electric and chiral conductivity by solving the above Maxwell equation using the Green's function method in cylindrical coordinates by considering that all source charges fly along the z -axis [44]:

$$\begin{aligned} B_\phi(t, \mathbf{x}) &= \frac{Q}{4\pi} \frac{v\gamma x_T}{\Delta^{3/2}} \left(1 + \frac{\sigma v\gamma}{2} \sqrt{\Delta}\right) e^A, \\ B_r(t, \mathbf{x}) &= -\sigma_\chi \frac{Q}{8\pi} \frac{v\gamma^2 x_T}{\Delta^{3/2}} e^A \left[\gamma(vt - z) + A\sqrt{\Delta}\right], \\ B_z(t, \mathbf{x}) &= \sigma_\chi \frac{Q}{8\pi} \frac{v\gamma}{\Delta^{3/2}} e^A \left[\Delta \left(1 - \frac{\sigma v\gamma}{2} \sqrt{\Delta}\right) \right. \\ &\quad \left. + \gamma^2 (vt - z)^2 \left(1 + \frac{\sigma v\gamma}{2} \sqrt{\Delta}\right)\right], \end{aligned} \quad (6)$$

in which Δ is defined as $\Delta \equiv \gamma^2 (vt - z)^2 + x_T^2$ and A is defined as $A \equiv (\sigma v\gamma/2) \left[\gamma(vt - z) - \sqrt{\Delta}\right]$; and

$$\begin{aligned} E_\phi(t, \mathbf{x}) &= \sigma_\chi \frac{Q}{8\pi} \frac{v^2 \gamma^2 x_T}{\Delta^{3/2}} e^A \left[\gamma(vt - z) + A\sqrt{\Delta}\right], \\ E_r(t, \mathbf{x}) &= \frac{Q}{4\pi} e^A \left\{ \frac{\gamma x_T}{\Delta^{3/2}} \left(1 + \frac{\sigma v\gamma}{2} \sqrt{\Delta}\right) \right. \\ &\quad \left. - \frac{\sigma}{v x_T} e^{-\sigma(t-z/v)} \left[1 + \frac{\gamma(vt - z)}{\sqrt{\Delta}}\right] \right\}, \\ E_z(t, \mathbf{x}) &= \frac{Q}{4\pi} \left\{ -\frac{e^A}{\Delta^{3/2}} \left[\gamma(vt - z) + A\sqrt{\Delta} + \frac{\sigma\gamma}{v} \Delta\right] \right. \\ &\quad \left. + \frac{\sigma^2}{v^2} e^{-\sigma(t-z/v)} \Gamma(0, -A) \right\}, \end{aligned} \quad (7)$$

where $\Gamma(0, -A)$ is the incomplete gamma function defined as $\Gamma(a, z) = \int_z^\infty t^{a-1} \exp(-t) dt$. It can be verified that with zero conductivity limit, Eqs. (6) and (7) return to the Lienard-Wiechert solution.

We have used the Monte-Carlo (MC) Glauber model developed by the PHOBOS collaboration [47] to calculate the spatial distribution of the source nucleons. MC Glauber model are useful for estimating EM fields in heavy ion collisions, and also with the help of Glauber model computations we can connect experimental data to collision centrality and other geometric quantities such

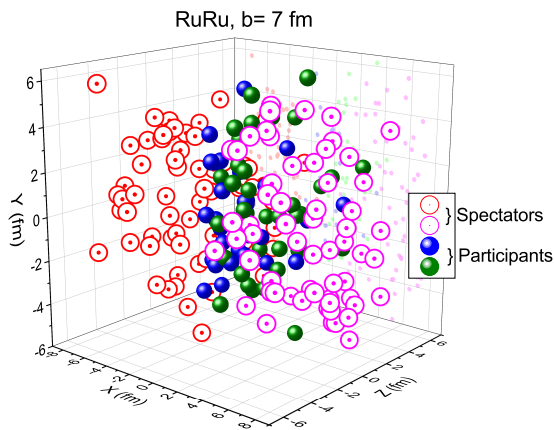


Figure 1. Initial geometry of a Ru+Ru collision event generated by the Monte-Carlo Glauber model for $b = 7$ fm and $\sqrt{s_{NN}} = 200$ GeV on the 3D plane.

as eccentricity, initial state anisotropy etc [46, 48–50]. To determine the spatial information of the source charges, a two-step calculation is performed in this model. The reaction plane is defined by the impact parameter and the beam direction, represented by x -axis and z -axis respectively. First, the centers of projectile and target nuclei are located at $x = \pm b/2$ for a given impact parameter b , and then it is employed to determine spatial positions of nucleons stochastically in the two colliding nuclei. The density profile of isobar nucleus have following Woods-Saxon (WS) distribution

$$\rho(x, y, z) = \frac{\rho_0}{1 + \exp\left[\frac{r - R(1 + \beta_2 Y_{20} + \beta_4 Y_{40})}{f}\right]}, \quad (8)$$

where ρ_0 is the nuclear density at the nucleus center, f represents the surface thickness parameter, and $Y_{nl}(\theta)$ represents spherical harmonic functions. Here β_2 , and β_4 are deformation parameters and they determine the deviation from a spherical shape of the nucleus. Taking into account these parameters allows us to obtain more realistic representations of spatial distribution of nucleons within the projectile and target nuclei. After determining the Woods-Saxon distribution information, the subsequent motions are then assumed to be along straight trajectories in the beam direction (i.e., in $+/-z$ directions). The collision between nucleons from projectile and target occurs if they satisfy $d \leq \sqrt{\sigma_{inel}^{NN}/\pi}$, where d is the distance in the transverse plane and σ_{inel}^{NN} denotes the inelastic cross section of nucleon-nucleon collisions. Those nucleons that do not partake in collisions are labeled as “spectators” while those that partake in collisions are labeled as “participants”.

In this work, we have used two isobar systems i.e., $^{96}_{44}\text{Ru} + ^{96}_{44}\text{Ru}$ (Ruthenium-96) and $^{96}_{40}\text{Zr} + ^{96}_{40}\text{Zr}$ (Zirconium-96) collisions. There are several WS parameter settings for two isobar nuclei. For the case of deformed nuclei structure, we use $R = 5.085$ fm and 5.020 fm for Ru and

Deformed Nuclei Case [51–53]			
	R_0	a	β_2
Ru	5.085	0.46	0.158
Zr	5.020	0.46	0.08
Halotype Nuclei Case [54, 55]			
Ru, n	5.085	0.523	0
Ru, p	5.085	0.523	0
Zr, n	5.021	0.592	0
Zr, p	5.021	0.523	0

Table I. Woods-Saxon parameters for Ru and Zr

Zr respectively, and $d = 0.46$ fm for both Isobar collisions at $\sqrt{s_{NN}} = 200$ GeV at RHIC. The deformation parameter β_2 is not confirmed yet and there are two cases for β_2 [51–53]. In one situation deformation parameter for $^{96}_{44}\text{Ru}$ is larger than $^{96}_{40}\text{Zr}$ ($\beta_2^{Ru} = 0.158$ and $\beta_2^{Zr} = 0.08$), while in other deformation parameter for $^{96}_{44}\text{Ru}$ is smaller than $^{96}_{40}\text{Zr}$ ($\beta_2^{Ru} = 0.053$ and $\beta_2^{Zr} = 0.217$) but in this paper we have only considered the first situation because the effect of deformation parameter has been studied in Ref. [28]. Apart from deformed nuclei structure there are also other WS distribution which can reflect neutron-skin effect, details of these parameters settings and effects are given and studied in [54, 55]. Among several WS parameter settings studied in [55] halotype nuclei has reproduce best experimental results for average number of charge particles, charged particle multiplicity (N_{ch}) and elliptical flow so we also considered halotype nuclei structure alongwith deformed nuclei structure. WS parameters used in this study are given in table I.

In Fig. 1, we show our initial charge distribution based on the Phobos MC Glauber on the 3D plane together with their XZ projections on the XY plane for $^{96}_{40}\text{Ru} - ^{96}_{40}\text{Ru}$ with $b = 7$ fm. Solid blue and green circles represent participant nucleons from the two colliding nuclei, while red and magenta open circles represent spectators that do not participate in inelastic scatterings. In order to assess whether a nucleon (proton) contributes to the electromagnetic field, we utilize the probability Z/A (44/96 for the Ru nucleus and 40/96 for the Zr nucleus). The evaluation of the electromagnetic field takes into account the contributions from the protons in both participants and spectators. It has been found that there is a tiny difference in magnitudes between considering only spectators and all nucleons. For instance, in Ru+Ru collisions at $b = 9$ fm, protons in the spectator alone produce around 4% less B_y than protons in the entire nucleus and almost similar yield is observed as well for Zr+Zr collisions in our setup. For calculating the electromagnetic field in the rest of this study, we perform event-by-event analysis over 100,000 MC Glauber events for each impact parameter (number of participants) setup to obtain a event-by-event geometric distribution of the source charges and relevant results.

The main objective is to study the correlation between

electromagnetic fields and plane angle formed by participants for zero-conductivity and finite conductivity cases, we use the definition of the n th plane participant plane angle represented by Ψ_n which can be calculated as

$$\Psi_n = \frac{\text{atan2}(\langle r_P^2 \sin(n\phi_P) \rangle, \langle r_P^2 \cos(n\phi_P) \rangle + \pi)}{n}, \quad (9)$$

where n can be 1,2,3 ... representing different flow harmonics, however in this work we only consider $n = 2$ because the second harmonics are most prominent and are tightly correlated to initial geometry distributions, r_P represents the displacement of participating nucleons from the field point \mathbf{r} and ϕ_P representing their corresponding azimuthal angle on the transverse plane. We also check the similarity and dissimilarity between zero-conductivity limit and finite conductivity system by calculating relative ratios defined by

$$X_c = 2 \frac{c^{Ru} - c^{Zr}}{c^{Ru} + c^{Zr}} \quad (10)$$

where c represents correlation $\langle \cos 2(\Psi_F - \Psi_2) \rangle$ or $\langle e\mathbf{F}^2 \cos 2(\Psi_F - \Psi_2) \rangle$ in our calculations. X_c close to zero represents similarity while away from zero represents dissimilarity between two isobar collision systems. Also by studying relative ratio trends we can get information about qualitative difference in zero-conducting case and finite conductivities case. If trends differ from each other more it will show difference in qualitative behaviour in vacuum scenario and finite conductivity scenario.

III. SIMULATION RESULTS AND DISCUSSIONS

A. Effects on Electromagnetic fields

1. Spatial Distributions:

In this subsection we show the numerical results of the contour plots of electric and magnetic fields compared between zero-conducting system and finite conductivity system (which have finite values of electric and chiral magnetic conductivity) for isobar collisions. As described in the previous section, the space-time evolution profile for electric charges for Ru+Ru and Zr+Zr is used for collisions at $\sqrt{s_{NN}} = 200$ GeV for different impact parameters. We use the Lienard-Wiechert solution for the case of zero-conductivity ($\sigma = \sigma_\chi = 0$), while for finite conductivity case Maxwell equations are solved to obtain the electromagnetic fields.

In Fig. 2 and 3, we show the contour plots of magnetic field $\langle B_{x,y,z} \rangle$ and electric field $\langle E_{x,y,z} \rangle$ in Ru+Ru collisions for $b = 7$ fm at $\sqrt{s_{NN}} = 200$ GeV. Each figure consists of two rows, in the first row the results from Lienard-Wiechert solution for zero-conductivity case are

presented and in the second row results in the presence of finite conductivities are presented. In our simulation for the case of finite conductivities, we take the values of conductivities as $\sigma = 5.8$ MeV and $\sigma_\chi = 1.5$ MeV same as Refs. [44, 46]. Here we notify that $\sigma = 5.8$ MeV is consistent to the lattice QCD calculations at top temperature of QGP produced at RHIC and it is expected that the expansion of QGP causes the decrease in σ together with temperature of medium. Currently there is no direct estimation towards choosing the σ_χ . Since the analytic solutions of Maxwell equations for electric and magnetic fields given in Eqs. 6 and 7 are obtained under the condition $\sigma \gg \sigma_\chi$ in Ref. [44], we take $\sigma_\chi = 1.5$ MeV as taken in the earlier work. The snapshot for zero-conductivity case is presented at $t = 0$ fm/c in the first row while the snapshot for finite conductivities case is presented at $t = t_Q$ fm/c in the second row for Ru+Ru collision at $b = 7$ fm at $\sqrt{s_{NN}} = 200$ GeV. We choose $t = t_Q$ fm/c for finite conductivity case because we observed maximum strength of field at this time as will be shown in upcoming Subsection III A 3. One can notice that spatial distribution of electric and magnetic field around $x = 0$ and $y = 0$ axes are symmetric when $\sigma = \sigma_\chi = 0$. Once we have finite conductivities then the symmetry of spatial distribution for electric and magnetic fields is broken that is they appear symmetric around $x = 0$ axis but asymmetric around $y = 0$ axis. This is due to the presence of σ_χ in E_ϕ and B_r in the electric field and magnetic field respectively. More details about broken symmetry of spatial distribution of the electric and magnetic fields are given in Refs. [44, 46]. We have also checked the spatial distribution for Zr+Zr collisions at $b = 7$ fm at $\sqrt{s_{NN}} = 200$ GeV and found that the trends for both cases are similar to those in Ru+Ru collisions.

2. Centrality dependence:

In this subsection we present the centrality dependence for the electric and magnetic fields in the vacuum case and the finite conductivity case and show comparison between them. Shown in Fig. 4 are the results for different impact parameters from central to non-central Ru+Ru collisions with two different WS parameters for vacuum (left panel) and finite conductivities case (right panel). Solid symbols with solid lines represent results for halotype WS parameters while open symbols with dashed lines are for deformed nuclei WS parameters for Ru in Ru+R collisions. Results show very little difference when the impact parameter is large but for small impact parameter almost no difference is found.

Shown in Fig. 5 are the results for different impact parameters from central to non-central collisions with halotype structure of Ru and Zr. Solid symbols with solid lines represent results from Ru+Ru collisions while open symbols with dashed lines are results from Zr+Zr collisions. Clearly one can see that the impact parameter plays important role on the strength of electric and mag-

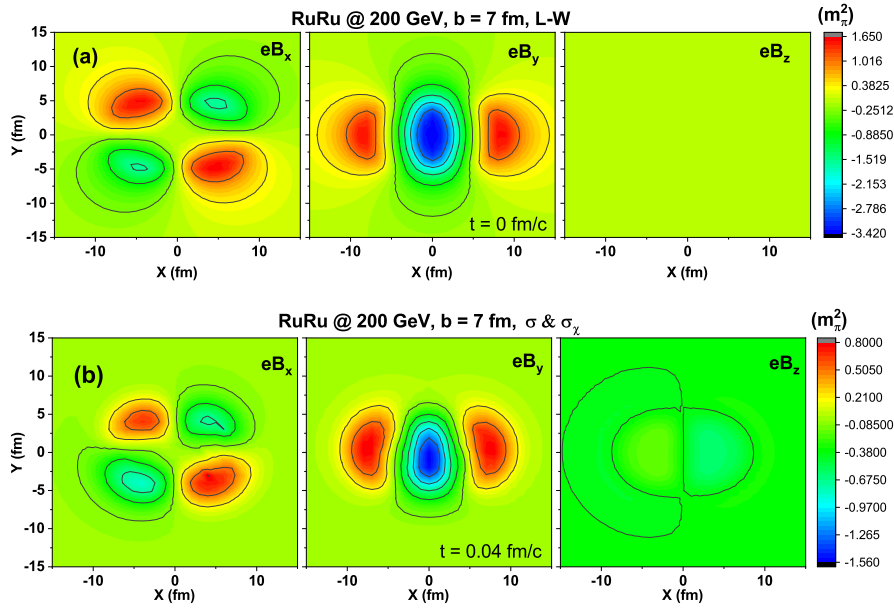


Figure 2. Spatial distribution of a magnetic field components ($eB_{x,y,z}$ in unit of m_π^2) in Ru+Ru for $b = 7$ fm at $\sqrt{s_{NN}} = 200$ GeV, compared between zero conductivity case (first row) vs. finite conductivities case (second row).

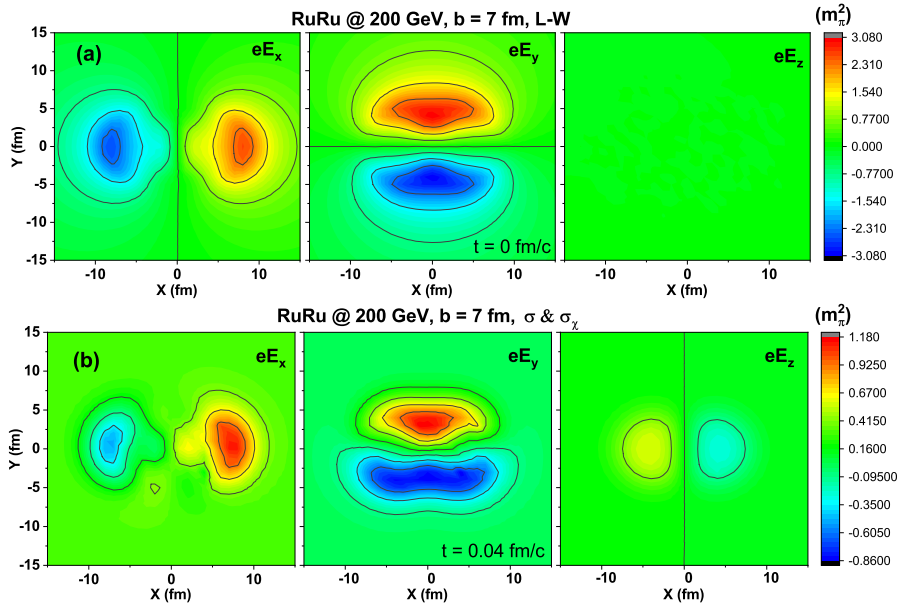


Figure 3. Spatial distribution of a electric field components ($eE_{x,y,z}$ in unit of m_π^2) in Ru+Ru for $b = 7$ fm at $\sqrt{s_{NN}} = 200$ GeV, compared between zero conductivity case (first row) vs. finite conductivities case (second row).

netic field components. For the case of zero-conductivity as shown in Fig. (5a) the results are similar to the results of electromagnetic fields for Au+Au and isobar collisions as in Refs. [1, 2] and [56] respectively. Moreover, the magnitudes of the magnetic and electric fields ($e\mathbf{F}$) follow $e\mathbf{F}_{Au} > e\mathbf{F}_{Ru} > e\mathbf{F}_{Zr}$ because of the decreasing number of protons in three collision systems respectively. Note that our simulation results show $|eB_x| \approx |eE_x| \approx |eE_y|$. For the case of finite conductivities as shown in Fig.

(5b), we present the impact parameter dependence of electric and magnetic field components at time t_Q . We clearly see that the presence of conductivities suppresses the strength significantly for eB_y and $|eB_y|$, however the magnitudes for $|eB_x|$ and $|eE_{x,y}|$ are still comparable in the vacuum and finite conductivity cases for small impact parameters. Longitudinal components of electric and magnetic field eF_z are always much smaller and consistent to zero in comparison with transverse components

for both vacuum and finite conductivity cases.

3. Time evolution:

In this subsection we show the time evolution of electric and magnetic fields in vacuum and finite-conductivities systems and show comparison between them. Since the dominant component is the magnetic field perpendicular to reaction plane so in Fig. 6 we show the time evolution of eB_y in the unit of m_π^2 for isobar collisions in the log-scale. From the figure we can see that for both isobar collisions although the magnitude for the vacuum case is large as compared to the conductivity case at the beginning but the former damps faster than the later. From the figure we also see that in case of conductivities, time evolution has a peak and reaches its maximum at $t_Q \sim 0.05$ (0.03) fm/c for $b = 8$ (4) fm in our calculations. So all the results which we present in this paper for the case of conductivities are at $t = t_Q$ fm/c because the maximum strength of field is achieved at this time. We also see that simulation results of Zr+Zr collisions are smaller as compared to Ru+Ru collisions due to less number of protons. We also compare the ratio $eB_y(Ru)/eB_y(Zr)$ in the bottom of the figure from Ru to Zr in two cases and they are around 1.1 consistent with the ratios of protons from Ru to Zr (Ru/Zr) showing the difference of 10% in magnetic field strength.

B. Azimuthal angle correlation between electromagnetic field and matter geometry

In this work we focus on taking into account the feedback effects from the electric and chiral magnetic conductivities and see their effects on the azimuthally fluctuating directions of electric and magnetic field. The effect of finite conductivities on spatial distribution and time behavior of the electromagnetic field in isobar collisions have been discussed in the previous subsection, we further extend our investigation to the correlation between azimuthally fluctuating electromagnetic fields with matter geometry characterized by participant plane and also give their effects on EM field related observables. So in the following subsection we give our exploration for these correlations.

1. Magnetic field and participant plane:

In this subsection we show the study of the correlation between azimuthal direction of magnetic field (Ψ_B) and participant plane (Ψ_2). The correlations have been studied in the presence of finite conductivities and compared to the zero-conductivity system. Before we give numerical results it is important to mention that the electric and magnetic field fluctuates strongly in azimuthal direction and magnitude on the event-by-event basis and so

does the participant plane. It is important to take into account the orientation of \mathbf{B} field with the corresponding matter geometry on event-by-event basis. Also the magnetic field induced effects which we observe occurs along or perpendicular to the direction of magnetic field, so it is important to determine the direction of \mathbf{B} field in accordance with experiments. By studying the correlation between Ψ_B and Ψ_2 we can determine the distribution of relative angle on event-by-event basis over many events and eventually we can give their effects on CME observable. Here we notify that usually the participant plane Ψ_n is rotated by π/n as shown in Eq. 9 to serve as proxy for the event plane measured in experiments [57] and also rotation is performed for the condition of sufficiently small elliptic flow [58], however in our model we do not consider this rotation. In our study we focus on seeing the effect of finite σ and σ_χ on the correlation between magnetic field and initial geometry of colliding system in Ru+Ru and Zr+Zr collisions.

In Fig. 7 we give the histograms of $\Psi_B - \Psi_2$ on event-by-event basis for Ru+Ru collisions (first row i.e., Fig. (7a)) and Zr+Zr collisions (second row i.e., Fig. (7b)) at $\sqrt{s_{NN}} = 200$ GeV for $b = 0, 4, 7, 10$ fm. In each row of figure we compare histograms obtained from the zero-conductivity case to the finite conductivities case. We calculate the Ψ_B at $\mathbf{r} = (0, 0, 0)$, and $t = 0$ fm/c for zero-conductivity case and $t = t_Q$ fm/c for finite conductivity case. The histograms given in Fig. (7a) for Ru+Ru collisions at $b = 0$ fm are almost uniform which represents Ψ_B and Ψ_2 are uncorrelated in fully overlapped collisions in both vacuum and finite-conductivity case. However for $b > 0$ fm as shown in figure for $b = 4, 7, 10$ fm histograms shows certain correlation between Ψ_B and Ψ_2 which have trends similar to Gaussian shape with wide widths and peaking at $\pi/2$ for both zero-conductivity and finite conductivities case. The peak of the histogram for zero-conductivity case is larger and its width is narrower as compared to finite conductivity case. This difference of peak and width is very minimal in peripheral collisions at $b = 10$ fm as there are very less number of participants at this impact parameter. The similar behavior is observed in Zr+Zr collisions as shown in the Fig (7b). The Fig. 7 is for deformed nuclei parameters, we checked that halotype nuclei parameters also have similar histograms.

Shown in Fig. 8 are the results for 2D distribution plots of Ψ_B and Ψ_2 for impact parameters $b = 0, 4, 7, 10$ fm at $\sqrt{s_{NN}} = 200$ GeV in Ru+Ru collisions. The scatter plots obtained in zero-conducting medium are presented in the first row (Fig. (8a)), while the scatter plots obtained in the conducting medium case are presented in the second row (Fig. (8b)). Again for $b = 0$ fm for both cases the distribution is uniform showing extremely weak correlation in fully overlapped collisions. However for $b = 4, 7, 10$ fm the distribution of scatter plot shows the concentration of distributions at $(\Psi_B, \Psi_2) = (\pi/2, 0)$ indicates the existence of correlation between two angles in both non-conducting and conducting medium. We observed the spread in Ψ_B is thinner in finite conductivity

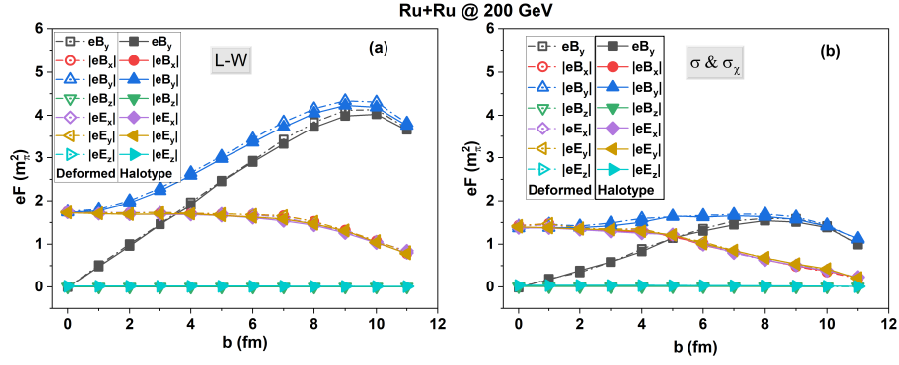


Figure 4. Comparison between $eF (m_\pi^2)$ for deformed (open symbols) and halotype (closed symbols) nuclei structure for Ru+Ru collision at $\sqrt{s} = 200$ GeV.

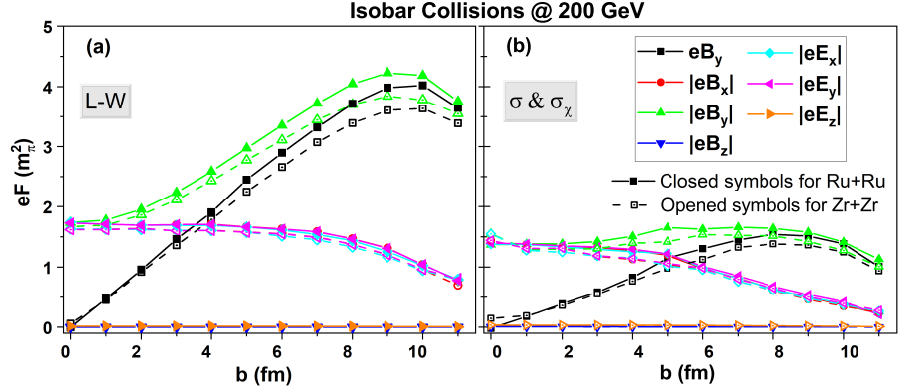


Figure 5. eF (in units of m_π^2) in isobar collisions (halotype) at $\sqrt{s_{NN}} = 200$ GeV as a function of impact parameter at $t = 0$ fm/c for zero conductivity case and $t = t_Q$ fm/c for finite conductivities case and compared between these two cases.

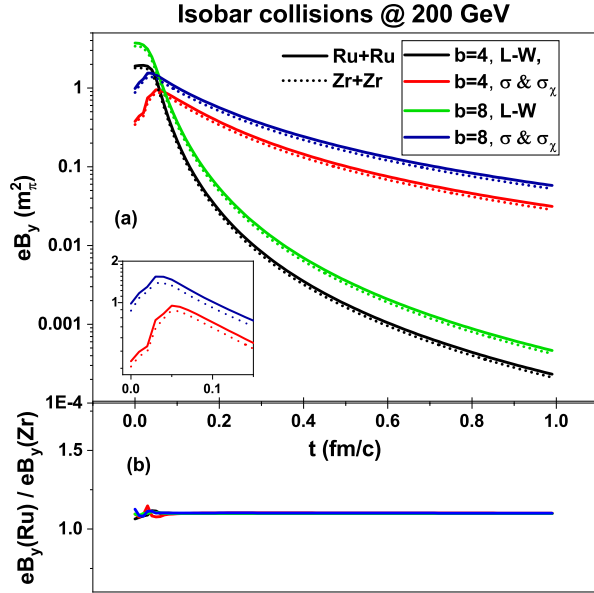


Figure 6. Time evolution of magnetic field eB_y in isobar collisions for $b = 4, 8$ fm at $\sqrt{s_{NN}} = 200$ GeV, compared between zero-conductivity case and finite conductivities case at $(0,0,0)$.

case as compared to zero-conductivity case. We have also checked 2D scatter plots for Zr+Zr collisions and the behavior is similar to that found in Ru+Ru collisions. Our histogram results and scatter plots between Ψ_B and Ψ_2 are similar to those reported in Refs. [33, 56]. The Fig. 8 is for deformed nuclei parameters, we checked that halotype nuclei parameters also have similar scatter plots.

Shown in the Fig. 9 is the correlation between Ψ_B and Ψ_2 in isobar collisions as a function of b in the first row (N_{part} in the second row) and compared the correlation between zero-conductivity and finite conductivities case. Results with solid symbol with solid lines are from halotype nuclei while open symbol with dotted lines are from deformed nuclei parameters. There is small difference found for both parameter settings which can also be seen from the relative ratios in Fig. (9b). From the figure we can also see that the correlation $\langle \cos 2(\Psi_B - \Psi_2) \rangle$ depends on centrality. Since spatial distribution of magnetic fields are symmetric around $x = 0$ axis but asymmetric around $y = 0$ axis in the presence of finite conductivities, we observe their effects on correlation as well on the transverse plane. On whole, results are consistent with the histograms and scatter plots given in Figs. 7 and 8 that is for small impact parameter and very large

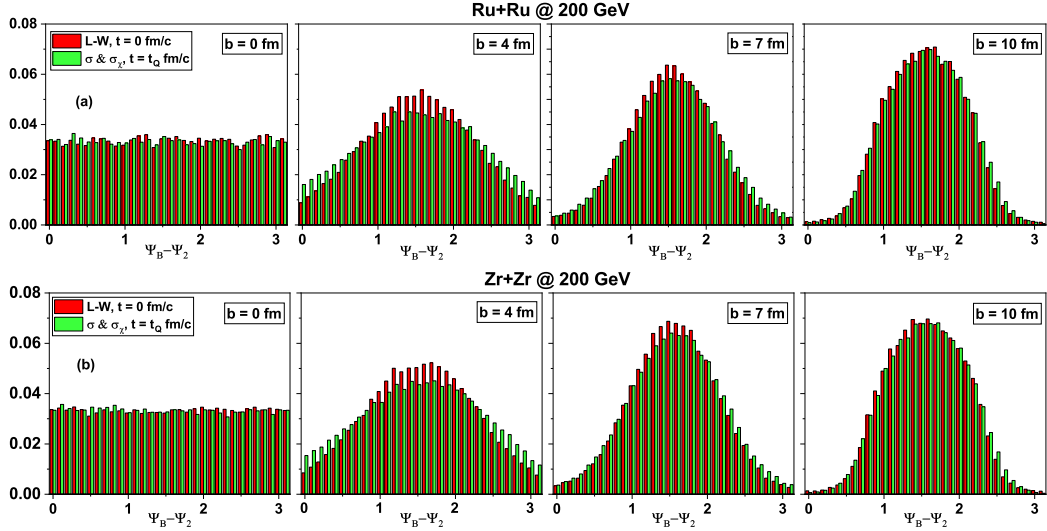


Figure 7. The histograms of $\Psi_B - \Psi_2$ on event-by-event basis and compared between vacuum case (L-W) and finite conductivity case for Impact parameter $b = 0, 4, 7, 10$ at $r = (0, 0, 0)$. Histogram results for Ru+Ru collisions are in the first row and for Zr+Zr collisions are in the second row at $\sqrt{s_{NN}} = 200$ GeV

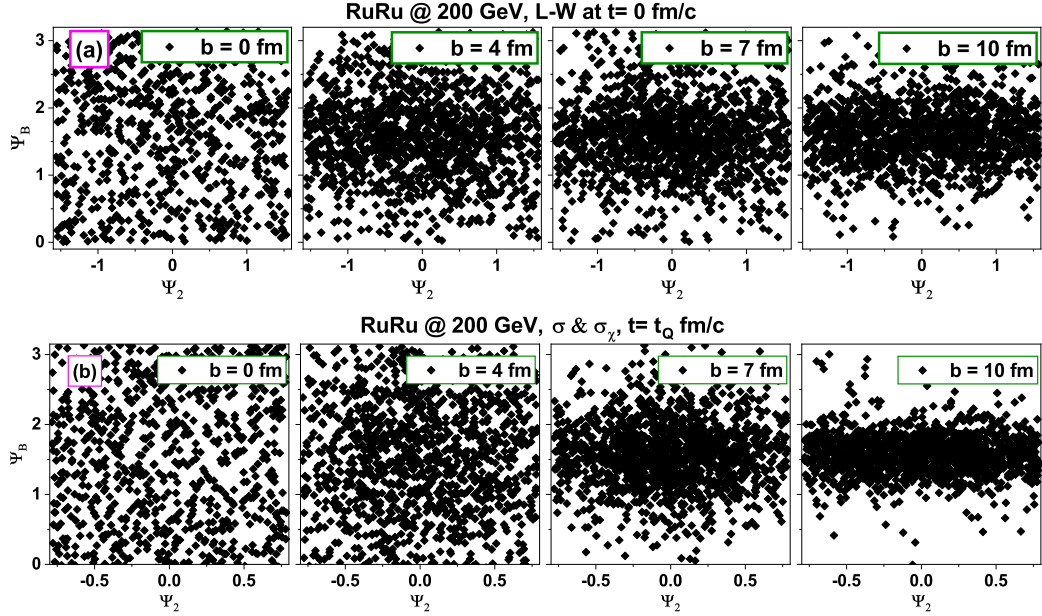


Figure 8. The scatter plots on $\Psi_B - \Psi_2$ plane in Ru+Ru collisions at $\sqrt{s_{NN}} = 200$ GeV for impact parameters $b = 0, 4, 7, 10$ fm and compared between zero-conductivity case (first row) to finite conductivities case (second row).

impact parameter the correlation is almost zero and very weak in zero-conductivity and finite conductivities cases. However, from figure we also see that at approximately $b = 7-9$ fm, the correlation $\langle \cos 2(\Psi_B - \Psi_2) \rangle$ reach their maximum value about -0.55 for vacuum case but the maximum value for finite conductivities case is smaller. From figure we also see that taking into account finite σ and σ_χ results are quantitatively different in magnitudes of correlation as compared to vacuum case but qualitatively consistent with the vacuum case. The results for vacuum case are almost similar to those given in Ref. [56].

Quantitatively the correlation at $(0,0,0)$ is suppressed to 40% in the presence of finite σ and σ_χ in intermediate impact parameter (at $b = 5$ fm) but this suppression decreases with the increasing impact parameter (suppression of 9% at $b = 10$ fm) for both Ru+Ru and Zr+Zr collisions. The relative ratio at origin point have similar trends for both cases but conducting medium case shows larger deviation from zero at smaller centralities. We notify that we have compared the results at the time $t = t_Q$ fm/c because we observed maximum value for magnetic field at this time for finite conductivities case, however

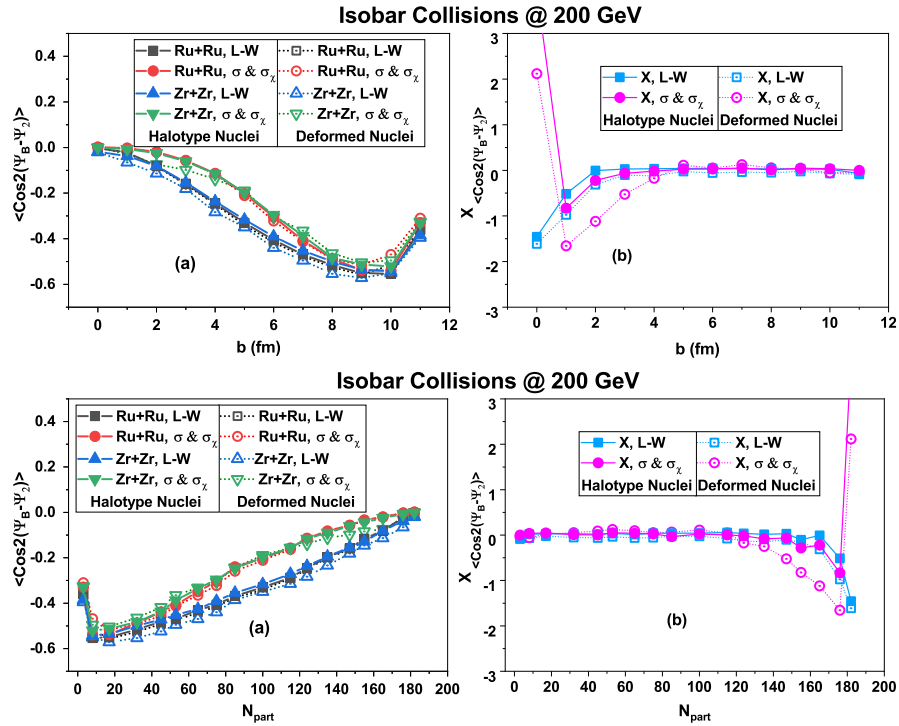


Figure 9. The correlation $\langle \cos 2(\Psi_B - \Psi_2) \rangle$ as a function of impact parameter b in the first row (N_{part} in the second row) in transverse plane respectively and their relative ratios in isobar collisions at $\sqrt{s_{NN}} = 200$ GeV, compared between zero-conductivity case and finite conductivities case.

we have also checked that if we take earlier time or later time then magnitude of the correlation is smaller.

According to the magnetic field induced effects, they show a directly proportional correlation with eB^2 along with $\langle \cos 2(\Psi_B - \Psi_2) \rangle$. The correlator $\langle eB^2 \cos 2(\Psi_B - \Psi_2) \rangle$ quantifies the effectiveness of magnetic field induced effect such as generating CME signal in γ correlator [33, 34]. So in Fig. 10 we show the results for $\langle eB^2 \cos 2(\Psi_B - \Psi_2) \rangle$ in Ru+Ru and Zr+Zr collisions as a function of impact parameter b in the first row (N_{part} in the second row) for vacuum scenario compared to the finite σ and σ_χ scenario. Results with solid symbols with solid lines represents for halotype nuclei settings while open symbols with dashed lines represents deformed nuclei settings. Comparing with Figs. 5 and 9 one can see that it inherits influence from both magnetic field and correlation. We see that by considering finite σ and σ_χ the magnitude is decreased 6 times but qualitatively the behavior is similar to vacuum case. We also see that maximum values of $\langle eB^2 \cos 2(\Psi_B - \Psi_2) \rangle$ is observed at earlier centrality in case of conductivities. The sizeable suppression can be observed for isobar collisions when compared to $\sigma = \sigma_\chi = 0$ case. We have also compared the relative ratios in two different scenarios and we found that although two scenarios differ quantitatively but qualitative trends are similar for $b > 4$ fm. From the results presented in Fig. 10, we can see that magnetic field in two different scenarios can play important role to the charge azimuthal correlation $\Delta\gamma$ as well accord-

ing to Eq. 1. Our study suggest that taking into account the feedback effects from QGP properties such finite conductivities can also suppresses the magnetic field induced effects such as CME signal. So when calculating the charge azimuthal correlation it is important to incorporate QGP properties such as σ and σ_χ .

2. Electric field and participant plane

In this subsection we give the brief study of the correlation between azimuthal direction of electric field (Ψ_E) and participant plane (Ψ_2) for completeness. As we have noticed in Fig. 5 that the electric field can also be comparably strong with the magnetic field. Possible charge distribution induced by strong electric field is an example of this. Similar to magnetic field we study the correlation $\langle \cos 2(\Psi_E - \Psi_2) \rangle$. In Fig. 11, we show the results as a function of b (N_{part}) in Ru+Ru and Zr+Zr collisions at $\sqrt{s_{NN}} = 200$ GeV for vacuum and conducting medium case at points (0,0,0) in the first row and (0,3,0) in the second row. As we noticed in previous section that halotype and deformed nuclei parameters have little difference on correlations and their relative ratios in our setup so in first row of Fig. 11 results are obtained by using halotype nuclei parameters and results in second row are obtained by using deformed nuclei parameters. In Fig. (11a), we calculate $\langle \cos 2(\Psi_E - \Psi_2) \rangle$ as function

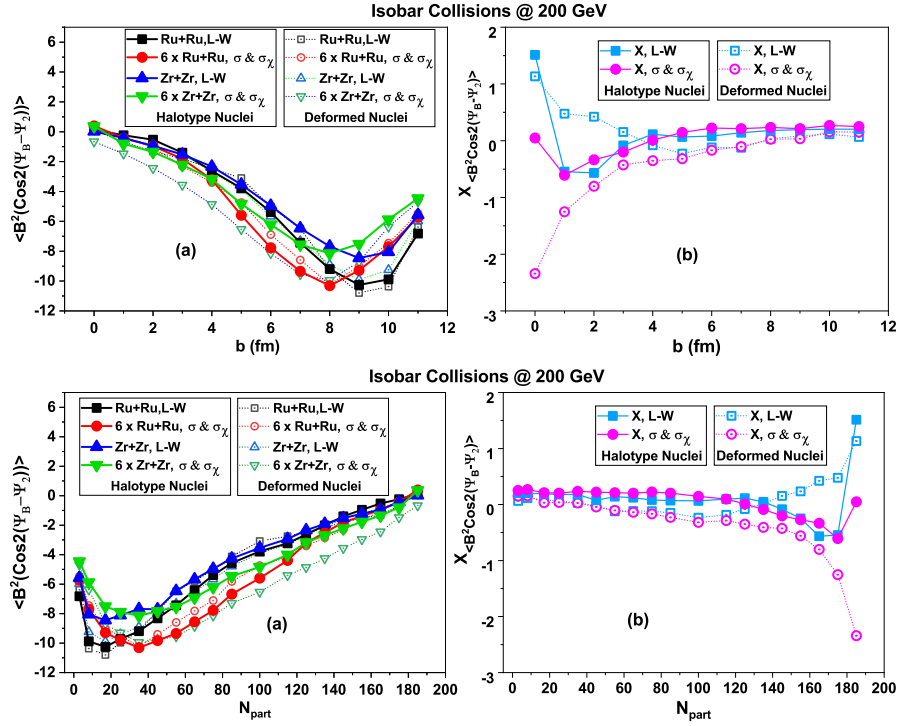


Figure 10. The correlation $\langle e\mathbf{B}^2 \cos 2(\Psi_B - \Psi_2) \rangle$ as a function of impact parameter b in first row (N_{part} second row) in transverse plane respectively and their relative ratios respectively in isobar collisions at $\sqrt{s_{NN}} = 200$ GeV, compared between zero-conductivity case and finite conductivities case..

of b and we can see that the correlation is very weak for Ru+Ru and Zr+Zr collisions for all impact parameters. The relative ratios shown in Fig. (11b) for both vacuum and medium case have similar trends for $b > 3$ fm ($N_{part} < 160$). However, this weak correlation can be understood together with the spatial distributions of electric field components given in Fig. 3 where we can see that at (0,0,0) electric field is very weak. The results shown in the second row of the Fig. 11 which corresponds to point (0,3,0), we see the sizeable correlation for zero-conductivity limit and finite conductivities case. We also observe enhancement of correlation in the presence of finite σ and σ_χ for small centralities. The relative ratios measured at this point for the two cases have shown similar trends for centrality dependence. So, we see that two scenarios behave similar qualitatively but differ in magnitude quantitatively.

Similar to the magnetic field, the observable quantity related to electric field can also be proportional to $e\mathbf{E}^2$ and $\langle \cos 2(\Psi_E - \Psi_2) \rangle$ so, in Fig. 12, we calculate the correlation $\langle e\mathbf{E}^2 \cos 2(\Psi_E - \Psi_2) \rangle$ as function of b (N_{part}) for Ru+Ru and Zr+Zr collisions at $\sqrt{s_{NN}} = 200$ GeV. We compared the results for vacuum case with the finite conductivity case at point (0,0,0) in the first row and at point (0,3,0) in the second row of figure. We see that it is very weak at (0,0,0) because the strength of electric field is also very weak at the origin point. The relative ratio at this point shows qualitatively almost similar trend for b fm (N_{part}) dependence. However, we notice ob-

servable effect at point (0,3,0) which can be understood together with the spatial distribution the electric field at this point. From the figure we also notice that the introduction of finite σ and σ_χ in system do affect the strength (4 times smaller) of correlation quantitatively however the qualitative picture is somewhat similar to the vacuum case. Relative ratios show different behavior at (0,3,0), for the case of finite conductivities relative ratios are near zero however for case of zero conductivity the relative ratio differs from zero. The results shown in figure suggest that while calculating observable quantity related to electric field, it is important to take into account feedback effects from the medium properties.

IV. SUMMARY AND OUTLOOK

In this study, we have conducted a systematic investigation on the effects of electric (σ) and chiral magnetic (σ_χ) conductivities on the impact parameter and space-time behaviors of electromagnetic fields generated in high-energy isobar collisions. Our results show that in transverse plane partially broken symmetry is observed for electric and magnetic fields in isobar collisions in the presence of finite σ and σ_χ , consistent with those observed in Au+Au collisions. Although the magnitude is smaller for the case of a conducting medium at earlier time but the lifetime of fields is much longer when com-

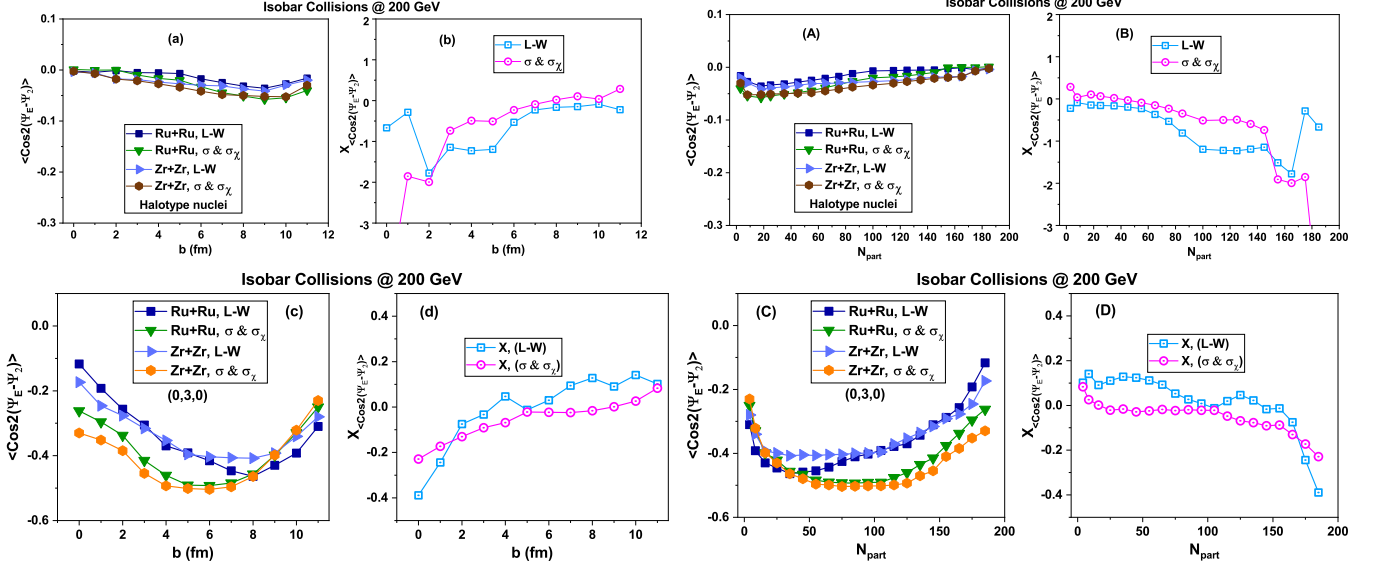


Figure 11. The correlation $\langle \cos 2(\Psi_E - \Psi_2) \rangle$ as a function of impact parameter b at two different positions in transverse plane that is $\mathbf{r} = (0, 0, 0)$ and $\mathbf{r} = (0, 3, 0)$ in first and second row respectively and their relative ratios respectively in isobar collisions at $\sqrt{s_{NN}} = 200$ GeV, compared between zero-conductivity case and finite conductivities case.

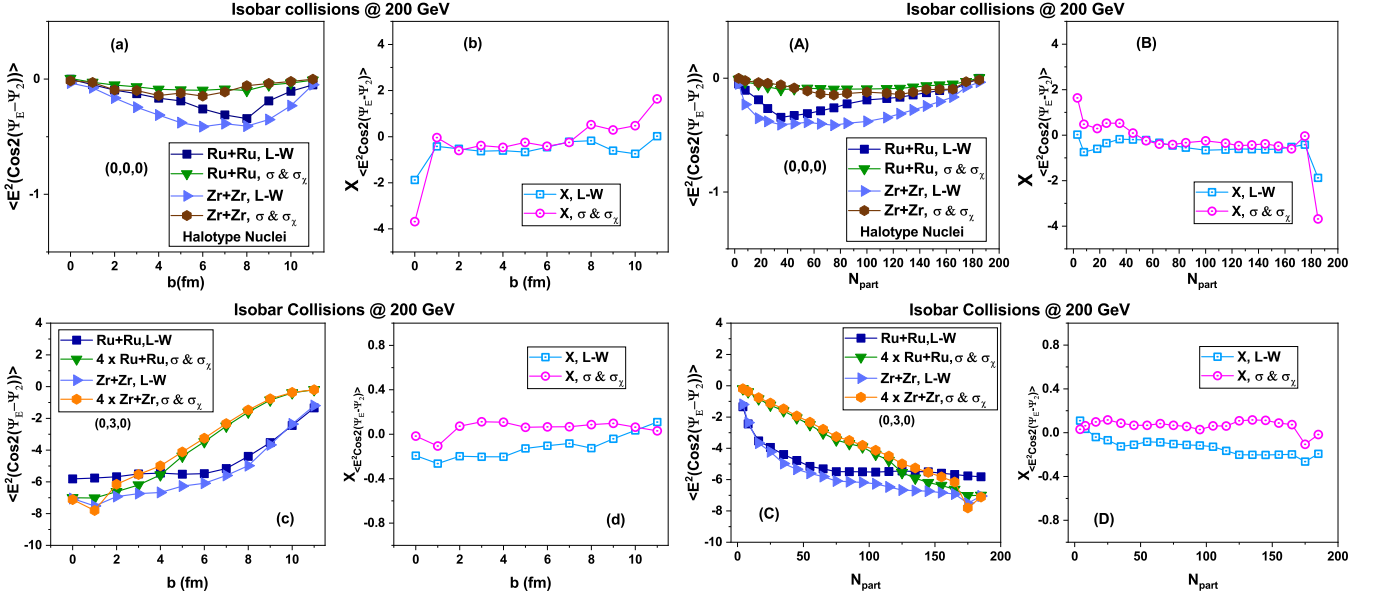


Figure 12. The correlation $\langle eE^2 \cos 2(\Psi_E - \Psi_2) \rangle$ as a function of impact parameter b at two different positions in transverse plane that is $\mathbf{r} = (0, 0, 0)$ and $\mathbf{r} = (0, 3, 0)$ in first and second row respectively and their relative ratios respectively in isobar collisions at $\sqrt{s_{NN}} = 200$ GeV, compared between zero-conductivity case and finite conductivities case.

pared to zero-conductivity limit (Lienard-Wiechert). We also confirm that magnetic fields differ by 10% even in the case of finite conductivities.

We also performed a detailed study on the azimuthal fluctuation of electromagnetic fields ($e\mathbf{F}$) in the presence of conductivities and studied their correlations with initial matter geometry i.e., $\langle \cos 2(\Psi_F - \Psi_2) \rangle$ and $\langle eF^2 \cos 2(\Psi_F - \Psi_2) \rangle$ on event-by-event basis. Comparison of the correlations has been presented between the

vacuum (L-W) and finite conductivities cases in this study. We see a sizeable suppression of the correlations in the presence of conducting medium, which reflects the importance of taking into account the medium properties such as conductivities while calculating the experimentally measurable observable such as $\Delta\gamma$ because quantities related to EM fields inherit influence from both the strength and the correlation between EM field direction and initial geometry. While the relative ratios measured

in this paper show similar trends for centrality dependence but large deviations are observed from central to mid-central collisions. We also take into account the two different WS nuclei parameters namely deformed nuclei and halotype nuclei and although they show difference in results but our calculation shows that the difference is not large and also qualitative behavior studied by relative ratios is similar for large centralities.

While in this work we have provided a quantitative understanding of the influence of finite σ and σ_χ on the electromagnetic fields as well as their azimuthal direction correlation with the initial geometry characterized by the participant plane in isobar collisions, it can be improved in several directions. It is needful to integrate these electromagnetic fields into a transport model or hydrodynamic model, from which one may draw a more solid conclusion about the consequent effects. In this study, we have only considered finite values for σ and σ_χ , but the values should change with the dynamical ex-

pansion in QGP. While in this work we only considered the participant plane one may also consider the spectator plane to see their correlation in the presence of conductivities. In future, it will be interesting to study the correlation between the fluctuations of electromagnetic anomaly ($\mathbf{E} \cdot \mathbf{B}$) and n th harmonic participant(or spectator) plane in the presence of conductivities. In an upcoming effort, we will extend our studies to these directions.

ACKNOWLEDGMENTS

We are grateful to University of Chinese Academy of sciences for providing platform to carry out simulations. Thanks to X.G. Huang and G.L Ma for discussions during the conference Chirality, Vorticity and Magnetic Field 2023. Thanks to Q.Wang, H. Mei, S.S. Cao, X.L. Sheng, D. Jian, H. Xu for discussions. This work is supported by the Ministry of Science and Technology of China.

-
- [1] A. Bzdak and V. Skokov, Phys. Lett. B **710**, 171 (2012), arXiv:1111.1949.
- [2] W.-T. Deng and X.-G. Huang, Phys. Rev. C **85**, 044907 (2012), arXiv:1201.5108.
- [3] V. Voronyuk *et al.*, Phys. Rev. C **83**, 054911 (2011), arXiv:1103.4239.
- [4] V. Skokov, A. Y. Illarionov, and V. Toneev, Int. J. Mod. Phys. A **24**, 5925 (2009), arXiv:0907.1396.
- [5] Y. Zhong, C.-B. Yang, X. Cai, and S.-Q. Feng, Adv. High Energy Phys. **2014**, 193039 (2014), arXiv:1408.5694.
- [6] D. E. Kharzeev, L. D. McLerran, and H. J. Warringa, Nucl. Phys. A **803**, 227 (2008), arXiv:0711.0950.
- [7] D. Kharzeev and A. Zhitnitsky, Nucl. Phys. A **797**, 67 (2007), arXiv:0706.1026.
- [8] K. Fukushima, D. E. Kharzeev, and H. J. Warringa, Phys. Rev. D **78**, 074033 (2008), arXiv:0808.3382.
- [9] K. Fukushima, D. E. Kharzeev, and H. J. Warringa, Phys. Rev. Lett. **104**, 212001 (2010), arXiv:1002.2495.
- [10] D. E. Kharzeev and D. T. Son, Phys. Rev. Lett. **106**, 062301 (2011), arXiv:1010.0038.
- [11] D. T. Son and P. Surowka, Phys. Rev. Lett. **103**, 191601 (2009), arXiv:0906.5044.
- [12] D. T. Son and A. R. Zhitnitsky, Phys. Rev. D **70**, 074018 (2004), arXiv:hep-ph/0405216.
- [13] M. A. Metlitski and A. R. Zhitnitsky, Phys. Rev. D **72**, 045011 (2005), arXiv:hep-ph/0505072.
- [14] D. E. Kharzeev and H.-U. Yee, Phys. Rev. D **83**, 085007 (2011), arXiv:1012.6026.
- [15] Y. Burnier, D. E. Kharzeev, J. Liao, and H.-U. Yee, Phys. Rev. Lett. **107**, 052303 (2011), arXiv:1103.1307.
- [16] Y. Burnier, D. E. Kharzeev, J. Liao, and H. U. Yee, (2012), arXiv:1208.2537.
- [17] H.-U. Yee and Y. Yin, Phys. Rev. C **89**, 044909 (2014), arXiv:1311.2574.
- [18] Y. Jiang, X.-G. Huang, and J. Liao, Phys. Rev. D **92**, 071501 (2015), arXiv:1504.03201.
- [19] STAR, B. I. Abelev *et al.*, Phys. Rev. Lett. **103**, 251601 (2009), arXiv:0909.1739.
- [20] STAR, B. I. Abelev *et al.*, Phys. Rev. **C81**, 054908 (2010), arXiv:0909.1717.
- [21] ALICE, B. Abelev *et al.*, Phys. Rev. Lett. **110**, 012301 (2013), arXiv:1207.0900.
- [22] STAR, L. Adamczyk *et al.*, Phys. Rev. C **88**, 064911 (2013), arXiv:1302.3802.
- [23] STAR, L. Adamczyk *et al.*, Phys. Rev. Lett. **113**, 052302 (2014), arXiv:1404.1433.
- [24] STAR, L. Adamczyk *et al.*, Phys. Rev. C **89**, 044908 (2014), arXiv:1303.0901.
- [25] CMS, V. Khachatryan *et al.*, Phys. Rev. Lett. **118**, 122301 (2017), arXiv:1610.00263.
- [26] S. Schlichting and S. Pratt, Phys. Rev. C **83**, 014913 (2011), arXiv:1009.4283.
- [27] F. Wang and J. Zhao, Phys. Rev. C **95**, 051901 (2017), arXiv:1608.06610.
- [28] STAR, J. Zhao, Nucl. Phys. A **982**, 535 (2019), arXiv:1807.09925.
- [29] A. Bzdak, V. Koch, and J. Liao, Lect. Notes Phys. **871**, 503 (2013), arXiv:1207.7327.
- [30] J. Zhao, H. Li, and F. Wang, Eur. Phys. J. C **79**, 168 (2019), arXiv:1705.05410.
- [31] H.-j. Xu *et al.*, Chin. Phys. C **42**, 084103 (2018), arXiv:1710.07265.
- [32] F. Wang, Phys. Rev. C **81**, 064902 (2010), arXiv:0911.1482.
- [33] J. Błoczyński, X.-G. Huang, X. Zhang, and J. Liao, Phys. Lett. B **718**, 1529 (2013), arXiv:1209.6594.
- [34] J. Błoczyński, X.-G. Huang, X. Zhang, and J. Liao, Nucl. Phys. A **939**, 85 (2015), arXiv:1311.5451.
- [35] S. Chatterjee and P. Tribedy, Phys. Rev. C **92**, 011902 (2015), arXiv:1412.5103.
- [36] S. A. Voloshin, Phys. Rev. Lett. **105**, 172301 (2010), arXiv:1006.1020.
- [37] STAR, M. Abdallah *et al.*, Phys. Rev. C **105**, 014901 (2022), arXiv:2109.00131.
- [38] STAR, Y. Hu, EPJ Web Conf. **259**, 13013 (2022), arXiv:2110.15937.
- [39] STAR, Y. Hu, Acta Phys. Polon. Supp. **16**, 44 (2023), arXiv:2208.09069.

- [40] W.-T. Deng, X.-G. Huang, G.-L. Ma, and G. Wang, Phys. Rev. C **94**, 041901 (2016), arXiv:1607.04697.
- [41] L. McLerran and V. Skokov, Nucl. Phys. A **929**, 184 (2014), arXiv:1305.0774.
- [42] K. Tuchin, Phys. Rev. C **88**, 024911 (2013), arXiv:1305.5806.
- [43] K. Tuchin, Phys. Rev. C **91**, 064902 (2015), arXiv:1411.1363.
- [44] H. Li, X.-l. Sheng, and Q. Wang, Phys. Rev. C **94**, 044903 (2016), arXiv:1602.02223.
- [45] I. Siddique, X.-L. Sheng, and Q. Wang, Phys. Rev. C **104**, 034907 (2021), arXiv:2106.00478.
- [46] I. Siddique, S. Cao, U. Tabassam, M. Saeed, and M. Waqas, Phys. Rev. C **105**, 054909 (2022), arXiv:2201.09634.
- [47] C. Loizides, J. Nagle, and P. Steinberg, SoftwareX **1-2**, 13 (2015), arXiv:1408.2549.
- [48] PHOBOS Collaboration, B. Alver *et al.*, Phys.Rev.Lett. **98**, 242302 (2007), arXiv:nucl-ex/0610037.
- [49] M. L. Miller, K. Reygers, S. J. Sanders, and P. Steinberg, Ann. Rev. Nucl. Part. Sci. **57**, 205 (2007), arXiv:nucl-ex/0701025.
- [50] B. Alver *et al.*, Phys. Rev. **C77**, 014906 (2008), arXiv:0711.3724.
- [51] P. Moller, J. R. Nix, W. D. Myers, and W. J. Swiatecki, Atom. Data Nucl. Data Tabl. **59**, 185 (1995), arXiv:nucl-th/9308022.
- [52] B. Pritychenko, M. Birch, B. Singh, and M. Horoi, Atom. Data Nucl. Data Tabl. **107**, 1 (2016), arXiv:1312.5975, [Erratum: Atom.Data Nucl.Data Tabl. 114, 371–374 (2017)].
- [53] Q. Y. Shou *et al.*, Phys. Lett. B **749**, 215 (2015), arXiv:1409.8375.
- [54] H.-j. Xu, H. Li, X. Wang, C. Shen, and F. Wang, Phys. Lett. B **819**, 136453 (2021), arXiv:2103.05595.
- [55] X.-L. Zhao and G.-L. Ma, Phys. Rev. C **106**, 034909 (2022), arXiv:2203.15214.
- [56] X.-L. Zhao, G.-L. Ma, and Y.-G. Ma, Phys. Rev. C **99**, 034903 (2019), arXiv:1901.04151.
- [57] G.-Y. Qin, H. Petersen, S. A. Bass, and B. Muller, Phys. Rev. **C82**, 064903 (2010), arXiv:1009.1847.
- [58] D. Teaney and L. Yan, Phys. Rev. **C83**, 064904 (2011), arXiv:1010.1876.